J. Fluid Mech. (2011), *vol.* 687, *pp.* 41–71.
doi:10.1017/jfm.2011.295

Particle dynamics in the channel flow of a turbulent particle–gas suspension at high Stokes number. Part 2. Comparison of fluctuating force simulations and experiments

Partha S. Goswami‡ and V. Kumaran†

Department of Chemical Engineering, Indian Institute of Science, Bangalore 560 012, India

(Received 2 July 2010; revised 24 June 2011; accepted 4 July 2011;
first published online 6 October 2011)

The particle and fluid velocity fluctuations in a turbulent gas–particle suspension are studied experimentally using two-dimensional particle image velocimetry with the objective of comparing the experiments with the predictions of fluctuating force simulations. Since the fluctuating force simulations employ force distributions which do not incorporate the modification of fluid turbulence due to the particles, it is of importance to quantify the turbulence modification in the experiments. For experiments carried out at a low volume fraction of 9.15×10^{-5} (mass loading is 0.19), where the viscous relaxation time is small compared with the time between collisions, it is found that the gas-phase turbulence is not significantly modified by the presence of particles. Owing to this, quantitative agreement is obtained between the results of experiments and fluctuating force simulations for the mean velocity and the root mean square of the fluctuating velocity, provided that the polydispersity in the particle size is incorporated in the simulations. This is because the polydispersity results in a variation in the terminal velocity of the particles which could induce collisions and generate fluctuations; this mechanism is absent if all of the particles are of equal size. It is found that there is some variation in the particle mean velocity very close to the wall depending on the wall-collision model used in the simulations, and agreement with experiments is obtained only when the tangential wall–particle coefficient of restitution is 0.7. The mean particle velocity is in quantitative agreement for locations more than 10 wall units from the wall of the channel. However, there are systematic differences between the simulations and theory for the particle concentrations, possibly due to inadequate control over the particle feeding at the entrance. The particle velocity distributions are compared both at the centre of the channel and near the wall, and the shape of the distribution function near the wall obtained in experiments is accurately predicted by the simulations. At the centre, there is some discrepancy between simulations and experiment for the distribution of the fluctuating velocity in the flow direction, where the simulations predict a bi-modal distribution whereas only a single maximum is observed in the experiments, although both distributions are skewed towards negative fluctuating velocities. At a much higher particle mass loading of 1.7, where the time between collisions is smaller than the viscous relaxation time, there is a significant increase in the turbulent velocity fluctuations by ∼1–2 orders

† Email address for correspondence: kumaran@chemeng.iisc.ernet.in

‡ Present address: CSIR Centre for Mathematical Modelling and Computer Simulation, Bangalore, India.

of magnitude. Therefore, it becomes necessary to incorporate the modified fluid-phase intensity in the fluctuating force simulation; with this modification, the mean and mean-square fluctuating velocities are within 20–30 % of the experimental values.

Key words: particle/fluid flow, turbulent flows

1. Introduction

Turbulent particle–gas flows are widely encountered in nature (avalanches, dust storms) as well as in industrial applications such as combustors, fluidized bed and circulating bed reactors. Since the carrier gas mass density is about three orders of magnitude lower than that of the particles, the mass loading is $O(1)$ even at small volume fractions of the particles. (This is in contrast to particle–liquid flows, where the densities of the continuous and dispersed phases are comparable.) Owing to this, the gas inertia is almost always negligible, and the dominant forces are the particle inertia, drag and lift forces due to the fluid, Brownian thermal fluctuations and colloidal forces. The interplay of these different forces depend on the particle size/diameter d. The Brownian forces (proportional to d^{-1}) and colloidal forces dominate for small particle diameters $\sim$1 μm (for particle mass densities around 1 kg m^{-3}), resulting in diffusive particle motion across fluid streamlines. In the 'tracer particle' (particles in the range 1–10 μm), the drag force, which is proportional to d, is larger than particle inertia or Brownian motion. Owing to this, the particles follow the fluid streamlines, and cross-stream diffusion is small. The force exerted by the particles on the fluid is also small compared with the fluid viscous forces. In the 'granular flow' regime, for particle diameters greater than $\sim$200 μm, the particle inertia is dominant, and the effect of fluid forces on the particles is small. In this case, it is a good approximation to solve the particle equations independently of the carrier fluid. In both the tracer particle and granular flow regimes, the equations of one of the phases (the fluid in the former and the particles in the latter) can be solved independently of the other phase.

In the intermediate regime of particle diameters in the range 10–200 μm, the particle inertia and the fluid drag and lift forces are comparable. This regime is industrially important, because particles in this size range are often used in combustors and reactors. It is also challenging, because there is a two-way coupling between the particle and fluid phase. The fluid exerts drag and lift forces, both due to the mean flow and turbulent fluctuations, on the particle phase. The particles, in turn, exert forces on the fluid and modify the fluid velocity fluctuations. This requires the equations for the two phases to be solved simultaneously.

The simplest 'two-fluid' models consider the particles and the fluid as two phases, which are coupled by an interaction force. Although these models can predict the relative velocity between the two phases, they do not directly provide the particle velocity fluctuations or the fluid turbulent velocity fluctuations. These fluctuations are of primary importance in modelling gas–particle flows in applications such as combustors and fluidized bed reactors, because the heat and mass transfer characteristics between the fluid and particles depend on the microscopic relative velocity between a particle and the surrounding fluid. The mean relative velocity is not adequate for modelling the microscopic transport rates. As a first step towards incorporating fluctuations, we have modelled the effect of the fluid turbulence on the particle velocity fluctuations (Goswami & Kumaran 2011). The fluctuating force

models include only one-way coupling, since the effect of the fluid on the particles is incorporated, but not the reverse effect of the particles on the fluid. Here, we test the predictions of the fluctuating force model against experimental results. In both simulation and experiments, we determine not just the mean and root mean square of the particle velocity fluctuations, but also the distribution function for the particle velocities, as a function of the wall-normal direction in a fully developed channel flow.

There have been a large number of simulation studies on particle-laden turbulent flows, but relatively few experimental studies. Most of the experimental studies have focused on investigating turbulence modulation due to the presence of the particles. A compilation of experimental data by Gore & Crowe (1989) indicated that small particles of size less than about a factor of 10 of the integral length scale of the fluid will attenuate the turbulence, while large particles will increase the turbulence intensity. Hetsroni (1989) attributed the effect of large particles to the wake formation. Tsuji & Morikawa (1982) used laser Doppler velocimetry (LDV) to study a particle-laden air flow in a horizontal pipe. They used 0.2 mm and 3.4 mm plastic particles with mass loading ratios up to 6. They have reported an attenuation of the streamwise turbulence intensities by the small particles whereas the large particles were found to augment the turbulence. The energy spectrum in the presence of the small particles showed that the spectrum was augmented at high frequencies and attenuated at low frequencies. They reported that the energy production by the mean shear stress was reduced as the mean velocity profiles became flatten, while the small-scale eddies were disturbed by particles. Tsuji, Morikawa & Shiomi (1984) performed an experiment on a vertical pipe using plastic particles with diameters ranging from 0.2 mm to 3 mm. Kulick, Fessler & Eaton (1994) performed experiments on a vertical channel using particles of Stokes number ranging from 0.57 to 3.0 with a mass loading up to 80 %, to investigate the turbulence attenuation. In their study, the Stokes number was expressed as the ratio of particle relaxation time to the Kolmogorov time scale. They observed greater attenuation in the transverse direction, and the attenuation was found to increase with increasing Stokes number and mass loading. The turbulence augmentation due to the presence of dispersed particle was reported by Sato & Hishida (1996), Suzuki, Ikenya & Kasagi (2000) and Kiger & Pan (2002). Paris (2001) has investigated the turbulent attenuation in a particle-laden channel flow. Turning to the effect of carrier phase turbulence on the discrete phase statistics, Fessler, Kulick & Eaton (1994) investigated the instantaneous particle concentration at the centre plane of a vertical turbulent channel flow. They performed experiments with particles of different Stokes number and found the maximum preferential concentration occurs when the Stokes number of the particles based on the Kolmogorov time scale is of order one. Khalitov & Longmire (2003) reported the results of their channel flow experiment mainly focusing on the two-point gas–particle and particle–particle correlation for Stokes number (based on an integral time scale) of 0.2–10, and observed that the gas–particle covariance becomes very small when the Stokes number is $\sim$5. Tanaka & Eaton (2008) have introduced particle momentum number (P_a) to categorize previous experimental measurements of wall-bounded turbulence to attenuation and augmentation. The number, defined as $P_a = S_t Re_L^2 (\eta/L)^3$, was derived using dimensional analysis of the particle-laden Navier–Stokes equations, where η and L are the Kolmogorov length scale and a representative large scale of the turbulence, respectively. Turbulence augmentation occurred for $P_a < 10^3$, attenuation occurs for P_a in the range $10^3 < P_a < 10^5$. Further increase in P_a corresponding to air flows laden with large particles resulted in turbulence augmentation. Yang & Shy (2005) reported augmentation due to preferential particle concentration around intense vortical

structures. Recently Tanaka & Eaton (2010) have reported small-scale turbulence modulation using a high-resolution particle image velocimetry (PIV) system.

We now turn to a brief discussion of the previous simulation work of turbulent fluid–particle suspensions. Squires & Eaton (1991) investigated the effect of isotropic turbulence on the concentration field of the heavy particle, and found that particle drift increased the eddy diffusivity. McLaughlin (1989) studied the deposition of aerosol particles in a turbulent channel flow applying direct numerical simulation (DNS). Particle trapping in boundary layer flow was investigated by Kallio & Reeks (1989). These investigators neglected the particle–particle collisions in their simulations. The effect of particle fluctuations on homogeneous turbulence was investigated by Squires & Eaton (1990) and Elghobashi & Truesdell (1993). Li & McLaughlin (2001) reported the effect of the forcing due to particles on the turbulent fluid velocity fluctuations, and the particle concentration profile in the case of a vertical channel flow. Wang & Squires (1996) performed a large eddy simulation (LES) to investigate the preferential particle distribution near the wall. They have performed one-way coupled simulation, without considering inter-particle collisions. Yamamoto *et al.* (2001) have performed the LES including inter-particle collision. Vreman (2007) has investigated the turbulence statistics in a particle-laden turbulent pipe flow for a solid mass loading up to 30 using DNS. For particles of size comparable or larger than the smallest undisturbed flow scales of the carrier phase, Bagchi & Balachandar (2003), Burton & Eaton (2005) and Zeng *et al.* (2008) performed fully resolved simulation for a single particle, whereas Pan & Banerjee (1997), Uhlmann (2008) carried out simulations for a collection of particles up to $O(1000)$. An overview of different approaches to model the particle-laden turbulent flows has been described by Goswami & Kumaran (2010*a*). In a dilute suspension, the different mechanisms that contribute to the turbulence modulation are enhanced dissipation due to the presence of particles, the transfer of kinetic energy to the fluid from the particles, and the formation of wakes and vortex shedding behind the particles (Balachandar & Eaton 2010).

The objective of the present work is to examine whether the fluctuating force simulation (FFS) procedure can be used to predict the dynamical properties of the channel flow of a gas–particle suspension. The FFSs have been formulated for the parameter regime where the particle relaxation time and the time between collisions are large compared with the correlation time of the turbulent velocity fluctuations. In the previous studies, the results of the FFS have been compared with the results obtained from DNS for both Couette flow (Goswami & Kumaran 2010*b*) and channel flow (Goswami & Kumaran 2011). Here, the results of the FFSs have been compared with experiments.

There are two reasons motivating this comparison. The first is that the DNS simulations incorporate only one-way coupling, where the effect of the fluid velocity fluctuations on the particles is incorporated, but not the reverse effect of the particles on the fluid. Since there is two-way coupling in the real experimental system, it is of interest to compare the FFSs with experimental results. Second, due to computational limitations on the total number of particles that can be simulated, the DNS simulations are restricted to relatively small gap thicknesses, with a maximum possible thickness of $\sim$4 mm. Owing to the small thickness, the fluid velocity is also much higher than that in experiments for equal Reynolds number, and the difference in the mean velocity of particles and fluid, which is comparable to the particle terminal velocity, is small compared with the particle mean velocity. Since the computational limitations do not apply to the FFSs, it is possible to carry out these simulation for much larger systems

with size comparable to those in experiments. This comparison is a critical test of the ability to make quantitative predictions from FFSs.

An important issue in the experiments is the polydispersity in the particle size distribution. It is found that polydispersity has a significant effect on the particle velocity fluctuations. This is because the particles with different diameters have different terminal velocities, and the difference in the terminal velocity drives collisions which generate particle velocity fluctuations (Kumaran & Koch 1993*a*,*b*). This mechanism for the generation of fluctuations is not present in the absence of polydispersity. We have investigated the mean particle velocity and intensity of the particle velocity fluctuation across the wall-normal direction of the channel. The distribution functions of the particle velocities have been computed at two different wall-normal positions of the channel: one at the centre and the other near the wall where the streamwise component of the fluid velocity fluctuation attains its maxima. Two different volume fractions have been analysed. At the lower volume fraction of 9.15×10^{-5}, the time between collisions is large compared to the viscous relaxation time, and we find good quantitative agreement between experiments and simulations. At the higher volume fraction of 8.2×10^{-4}, there is a significant increase in the intensity of the turbulent fluctuations due to the particles, and it is necessary to incorporate this increase into the FFSs. Experimental facilities and techniques have been described in § 2. Section 3 describes and interprets the results. Conclusions are given in § 4.

2. Experimental method

The experimental facility consists of a vertical channel of aspect ratio ∼10, so that the flow in the centre of the channel is two dimensional. The particles (glass beads) are fed into the channel using a vibratory particle feeder. In order to determine the fluid velocity using PIV, it is necessary to introduce seed droplets of diameter ∼1–2 μm, which follow the fluid streamlines and can be imaged. The seed droplets are introduced using a fog injection system. High-resolution PIV is used for determining the fluid and particle velocities, and a computer-controlled data acquisition system is employed for capturing and storing the experimental results.

2.1. *Channel description*

All of the experiments are conducted in the vertical rectangular channel shown in figure 1, which is 38 cm in width (spanwise direction) and 4 cm in thickness (cross-stream direction). Owing to the high aspect ratio of the channel, the flow in the central region (away from the end walls in the spanwise direction) can be considered to be a two-dimensional flow.

The channel consists of an air inlet section of height 15 cm, a flow conditioning section of height 40 cm, a flow development section of height 1 m and test section of height 50 cm. The particle feeding arrangement is fitted on the top of the air inlet section. The channel is mounted on the iron platform with support from the four sides. Air is supplied to the channel from the centrifugal blower (Giliyal Industry, Bangalore, Karnataka, India), which is driven by a 5 HP three-phase induction motor at 2880 rpm. The capacity of the blower is 1000 $m^3\ h^{-1}$, with a static head 600 mm water gauge. A gate valve was used to control the air flow rate.

Air enters the channel through four inlet pipes and then through six holes 2 inches in diameter, placed opposite each other in the wall of the channel as shown in figure 1. This type of air inlet arrangement avoids the flow separation due to sudden expansion of the flow from the inlet tube to the channel. The input of air from the side also

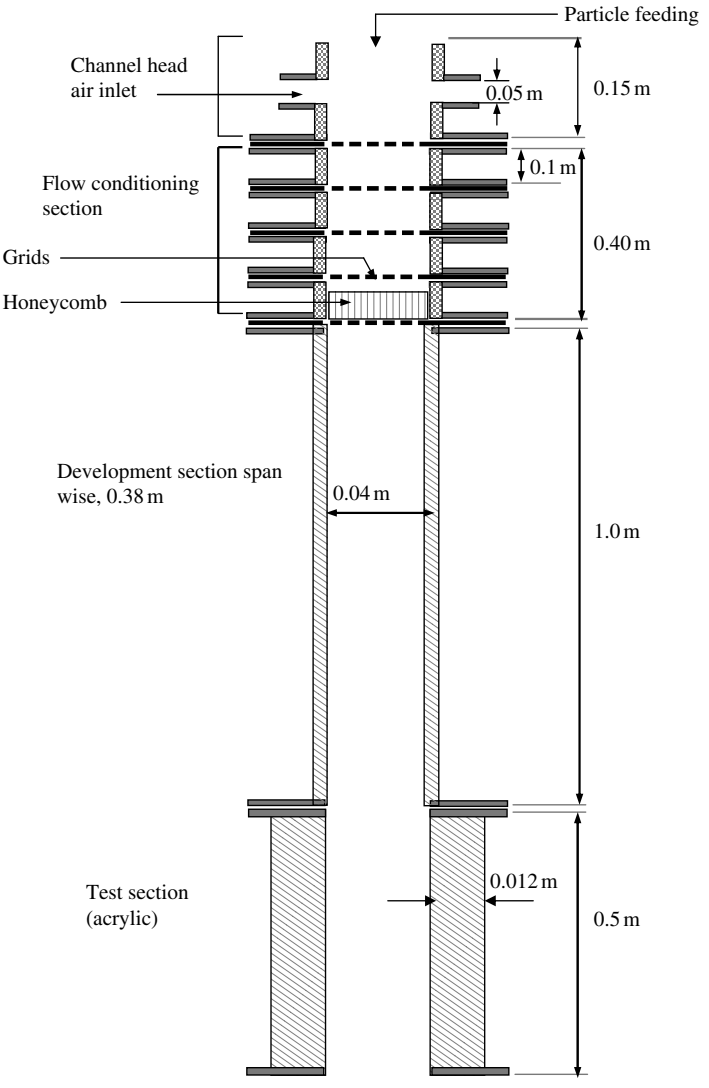

FIGURE 1. Internal description of the channel facility.

allows the vibratory particle feeder to be placed on the top of the channel. In the air inlet section, a plastic mesh of 2 mm mesh size is used to break up the large vortices, since vortices may lead to the accumulation of the particles at the centre plane of the channel.

Below the air inlet section, there is a flow conditioning section of height 40 cm as shown in figure 1, which consists of four plastic grids of 2.25 mm square holes uniformly spaced at 10 cm interval. After the third grid, one honeycomb structure made of aluminum with 6 mm cell size and 0.068 mm wall thickness (supplied by Honeycomb India Private Limited) is placed to suppress the feeder-induced or large-vortical-structure-induced transverse motion of the particles.

Downstream of the flow conditioning section, there is the development section. This section extends for a length of 1 m, which is sufficient to achieve fully developed

Particles	Particle diameter (μm)	Stokes relaxation time (s)	Corrected relaxation time (s)	Transition length for particle (m) $U_g = 2$ m s^{-1}	$U_g = 4$ m s^{-1}
Glass beads	60	0.028	0.024	0.162	0.298
($\rho_p = 2500$ kg m^{-3})	80	0.051	0.051	0.288	0.514
	120	0.114	0.075	0.619	1.059
	140	0.155	0.093	0.814	1.371

TABLE 1. Particle diameter and required transition length. In calculating the transition length we have considered the distance that the particle will travel before achieving 99 % of the terminal velocity.

turbulent flow at the entrance of the test section. We have ensured that the residence time of the particles in development section is nearly 1.5–2 times higher than the time required for the particle to reach its terminal velocity, calculated based on the centre-line gas velocity and the nonlinear drag law (3.3) as shown in table 1. The development section is constructed from 3 mm thick aluminum plates. To ensure that the boundary layer is turbulent, rough sand paper is fixed at the entrance of the development section.

Downstream of the development section is the 50 cm long test section, with walls of 12 mm thick acrylic sheet. One of the sidewalls of the test section can be removed to access the inside wall of the test section during the cleaning operation to remove the solid particles deposited on the wall. Particles are collected in a recycle bin and reused. In order to capture the small particles, we used a filter of pore size 100 μm at the mouth of the exit pipe attached to the recycle bin.

To feed the solid particles uniformly into the channel and control the flow rate of the particles, we have used a vibratory particle feeder, which has a static upper part and a vibrating lower part. A micro-vibrator (manufactured by Italvibras Giorgio Silingardi S.p.A.) is fixed to the lower vibrating part. During the experiment, we have changed the amplitude of vibration to change the feed rate of the particles, while keeping the frequency constant. In addition to controlling the amplitude of the micro-vibrator, we have also made an arrangement to control the effective flow area for the particles by putting stainless steel wire mesh of pore size 300 μm inside the lower part of the feeder.

2.2. *Particle image velocimetry*

Non-intrusive measurements of the velocity field were made using a two-dimensional PIV facility (IDTpiv, USA). The PIV unit consisted of a Nd:YAG laser (Solo-III, New-Wave research), laser sheet generating optics and a CCD camera (sharpVISION^{TM} 1400-DE with resolution of 1360 × 1030 pixels). One lens (micro Nikor) with 60 mm focal length was attached to the camera. A timing interface unit (IDT) was used to control the trigger timing signals to the laser and camera. Image acquisition and processing have been done using proVision (IDTpiv) software on a Sony desktop computer model PCV-7762. In order to obtain velocity data with high spatial resolution, the package includes a novel mesh-free second-order accurate algorithm, which has been described in detail by Lourenco & Krothapalli (2000). To obtain the velocity field, the images are subdivided into sub-images, and the average spatial shift of particles was calculated from one image to the next by statistical correlation techniques. Sub-pixel resolution was achieved by means of a Gaussian interpolation

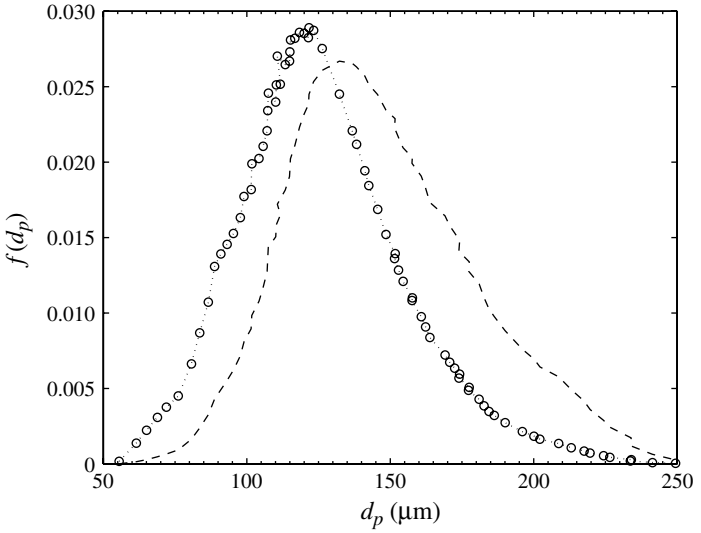

FIGURE 2. Particle size distribution: ○, number-based distribution; - -, volume-based distribution.

procedure. An error checking algorithm was enabled in the software proVISION-II to ensure that the velocity vector obtained after the image processing was valid. A detailed discussion of the processing algorithm and comparison with standard PIV algorithms can be found in Lourenco & Krothapalli (2000) and Krothapalli *et al.* (2003). The authors have described the superiority of the algorithm from the view point of 'bias' or 'peak-locking' by providing a continuous distribution of the velocity in a highly turbulent flow, although Hwang & Eaton (2006) found little effect of peak-locking on turbulence statistics for their particle-laden homogeneous turbulent flow experiment.

A high-output fog generator Satan ZF-3000 with a multi-function control system was used to generate the fog, which was used as the gas-phase tracer element. Arrangements have been made to seed the gas phase continuously at a high seeding level. The fogger outlet was connected to the inlet of the blower through a distribution box to seed the gas phase continuously. Small droplets with significant Brownian motion are trapped at the bends of the pipe lines connected from the blower to the channel and only droplets of size 1–2 μm reach the test section of the channel.

2.3. *Experimental procedure*

The glass particles were procured from Potters Industries Inc. (through Continental Trading Corp, Chennai, India). The distribution function of the particle diameter is shown in figure 2. The number-based mean particle diameter is 123.3 μm with standard deviation in diameter of 20.5 %.

An issue of importance in the experiments is the effect of humidity on the dynamics of the particle phase. Khalitov & Longmire (2004) reported that a humidifier is necessary in the main air flow line, because electrostatic effects on particle interactions increase as the humidity level decreases. The authors analysed the effect of the relative humidity on the gas–particle correlation, and found that there was an increase in the gas–particle correlation of 30 % for increasing relative humidity from 75 % to 90 %.

We carried out our experiments under atmospheric conditions, where the relative humidity was ∼50 %, without any separate humidification arrangement. Owing to the hygroscopic nature of the glass particles, if the contact time of the glass beads with humidified air (air mixed with fog as tracer) is high, the glass beads form soft agglomerates. This changes the physical parameters such as the effective diameter or viscous relaxation time of the particle. Therefore, at the end of each run, it was necessary to dry the glass beads by heating at 45–50 °C. After heating, the beads were cooled down in a closed vessel to room temperature before the experiments.

Before performing the experiment for gas–particle flow, calibration was done by opening the removable window of the test section and putting graduated scale at the plane of the laser sheet. Then the window was closed and we started the air blower, fogger and the particle feeder. After approximately 15 s when the flow became steady, the image acquisition was started at a rate of five pairs of frames per second. Depending on the availability of the memory of the CPU, it is possible to acquire up to 200 pairs of frames in one run, which is equivalent to 40 s of flow time. Particles are collected from the recycle bin and weighed in a weighing machine with resolution of 50 g. After completion of each set of the experiments, the channel was cleaned by a hand blower. The wall of the test section was cleaned by opening the removable window.

The PIV measurements were taken in the wall-normal plane (x–y). The measurement zone was 30 mm × 40 mm in streamwise and wall-normal direction. After acquiring the raw images, a thresholding technique was used to separate the image into two separate images, one containing the solid particles and the other containing the tracers, as described in the following section.

2.4. *Image processing for multiphase flow*

The image processing of the multiphase flow is complicated due to the presence of the large particles and the small tracer droplets in the same image frame. If such a frame is processed by the PIV image-processing software (proVision), the large particles will have an influence on the image correlation of the small tracer particles. Therefore, it is necessary to identify two different types of particles in the acquired images and separate them before processing to obtain the instantaneous velocities of the different phases. Researchers have developed different methodologies to separate the phases in PIV images, such as separation based on colour, image intensity, particle sizes in the image, etc. A brief overview has been given by Khalitov & Longmire (2002) and Goswami (2009).

In the present work, we have used the size and intensity-based separation procedure (Paris & Eaton 1999; Khalitov & Longmire 2002). For separating the images of the tracer particles and the dispersed phase, we have used the open-source image processing software imageJ (Rasband 2006). In the first step, we threshold the image containing the tracer and the dispersed phase by a pixel count of 180–200 out of a maximum of 255 in 8-bit greyscale. This operation removes all of the background pixels and most of the tracers, leaving high-intensity peak pixels of the tracers and the pixels associated with the dispersed particles as shown in figure 3(*a*). A second screening is done by fixing a minimum size in the binary image obtained from the previous step. This step removes all of the tracer particles and leaves the dispersed solid particles as shown in figure 3(*b*). After locating the large dispersed particles in this manner, the original grey image is consulted to find the centre of mass of the

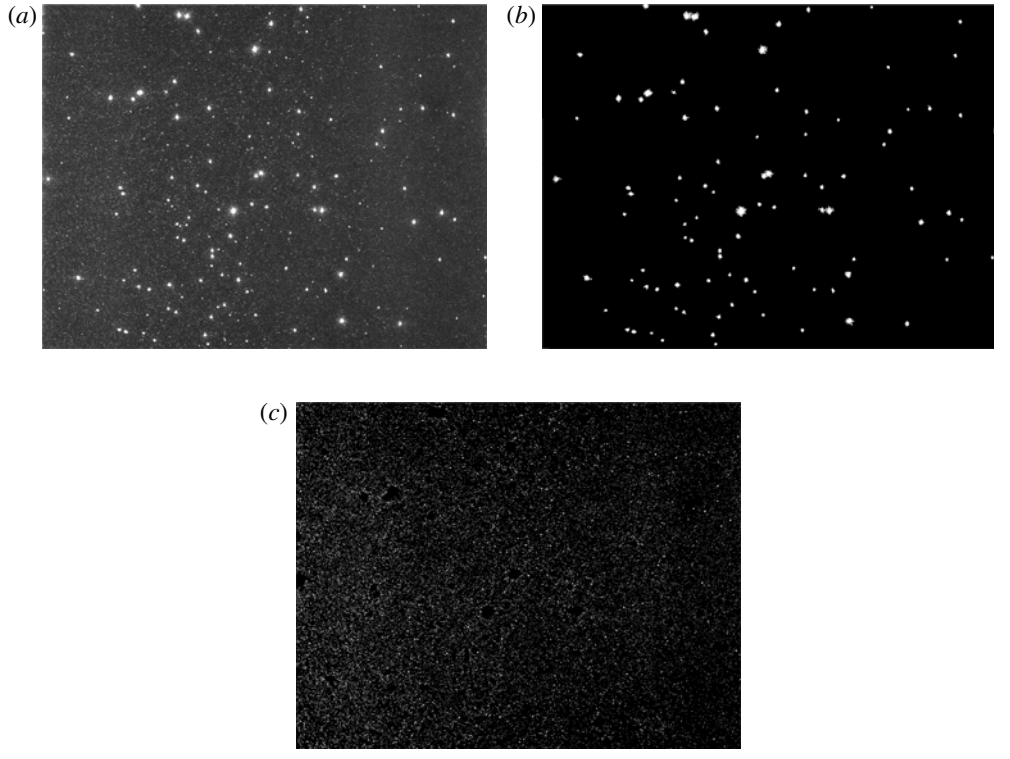

FIGURE 3. Processing of the PIV image: (*a*) original image; (*b*) image of solid particles; and (*c*) image of tracers.

particle, which is calculated using the moment method given in

$$\boldsymbol{X}_c = \frac{\sum_k \boldsymbol{X}_k I_k}{\sum_k I_k}. \tag{2.1}$$

A particle-tracking algorithm has been developed to measure the velocity field of the dispersed phase once the particle centres are detected. In the particle-tracking algorithm, the identity of the particles has to be matched in successive frames. Owing to the particle motion in the direction perpendicular to the plane of laser sheet, the number of particles in the consecutive frames are not the same. Therefore, we have considered the frame that contains the lowest number of particles as the base frame, and for each particle in this frame, we create a search window in the other frame and search for the matching partner. The size of the search window depends on the velocity field of the dispersed phase and the time separation of the consecutive frame, also the size window is fixed in such a way that the possibility of finding more than one partner is small. For our experiments, we have used a circular window of diameter 5 pixels. If there is more than one particle in the search window, we consider the nearest neighbour as the matching partner. Once the displacement is found, the velocity of the particle are obtained by dividing the displacement with the time separation of the frame assigned at the time of image acquisition. The

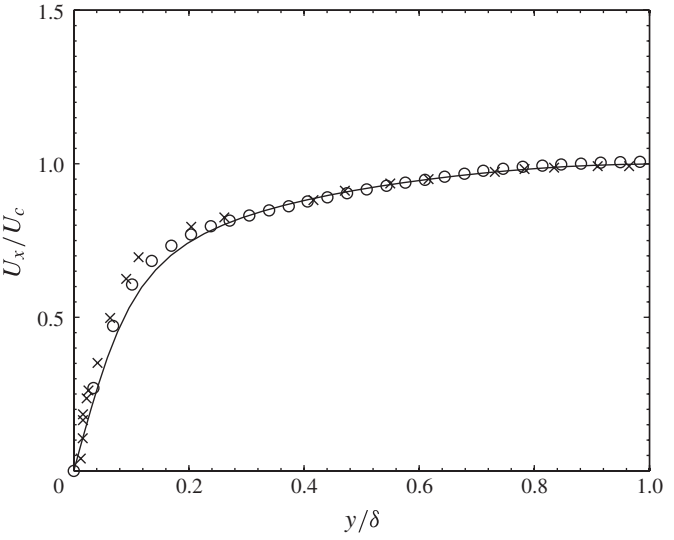

FIGURE 4. Gas-phase mean velocity profile from experiment and DNS. ∘, PIV experiment, $Re_c = 2021.14$; —, DNS, $Re_c = 2021.14$; ×, Niederschulte, Adrian & Hanratty (1990), $Re_c = 3221.5$.

velocities calculated in this manner are assigned to the particles of the first image frame. This algorithm works best when the particle–particle distance is larger than the displacement of the particles.

The next image-processing step is to subtract the image frame containing only the large particles from the original image. This step produces the image frame containing only the tracer particles as shown in figure 3(*c*). To obtain the gas-phase velocity, these images are processed by proVision^{TM} image-processing software provided by IDT. The interrogation window used for the analysis was 24 × 24 for the experiments with only air flow (results were the same with 32 × 32 as well), 32 × 32 for the experiments with lower solid volume fraction and 64 × 64 (with an adaptive window flag on in the software) for the experiments containing higher solid volume fraction.

2.5. *Validation of PIV results for single phase flow*

The validation of the PIV results have been carried out by comparing with the results obtained from DNS for the flow of gas without particles. For the PIV analysis of the raw image, a 24 × 24 correlation window has been used, and the image domain is subdivided into 100 grids to obtain mean velocities at 100 wall-normal positions. Figure 4 shows the mean gas velocity obtained from the PIV experiment and the DNS at Reynolds number 2021.1, based on the air velocity at the centre of the channel. Figure 5 shows the comparison of the streamwise and transverse mean-square velocities, and the second moment of the fluid velocity fluctuation has been compared in figure 6.

3. Results for multiphase flow

In this section, we describe the particle- and gas-phase measurements for two solid volume fractions, the first for low solid volume fraction where the viscous relaxation time of the particle is lower than the particle–particle collision time, and the second

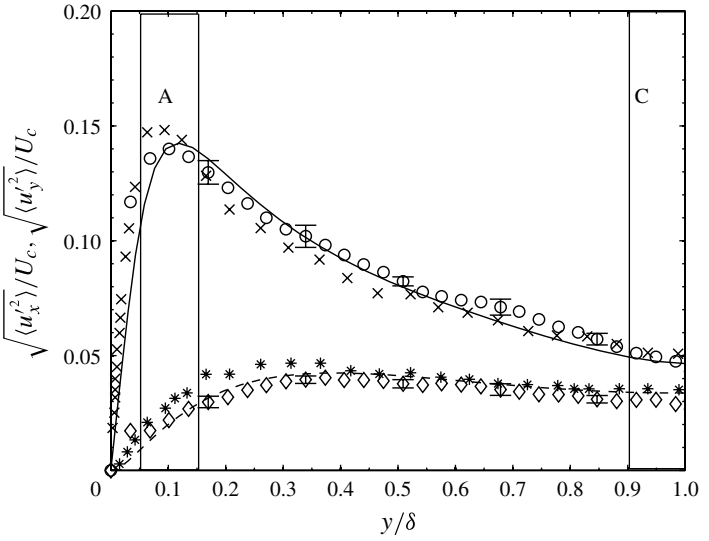

FIGURE 5. Gas-phase turbulent intensity obtained from experiment and DNS. (∘), $\sqrt{\langle u_x'^2\rangle}/U_c$, PIV, $Re_c = 2021.14$; (—), $\sqrt{\langle u_x'^2\rangle}/U_c$, DNS, $Re_c = 2021.14$; ×, $\sqrt{\langle u_x'^2\rangle}/U_c$, Niederschulte *et al.* (1990), $Re_c = 3221.5$; (◇), $\sqrt{\langle u_y'^2\rangle}/U_c$, PIV, $Re_c = 2021.14$; (- -), $\sqrt{\langle u_y'^2\rangle}/U_c$, DNS, $Re_c = 2021.14$; ∗, $\sqrt{\langle u_y'^2\rangle}/U_c$, Niederschulte *et al.* (1990), $Re_c = 3221.5$.

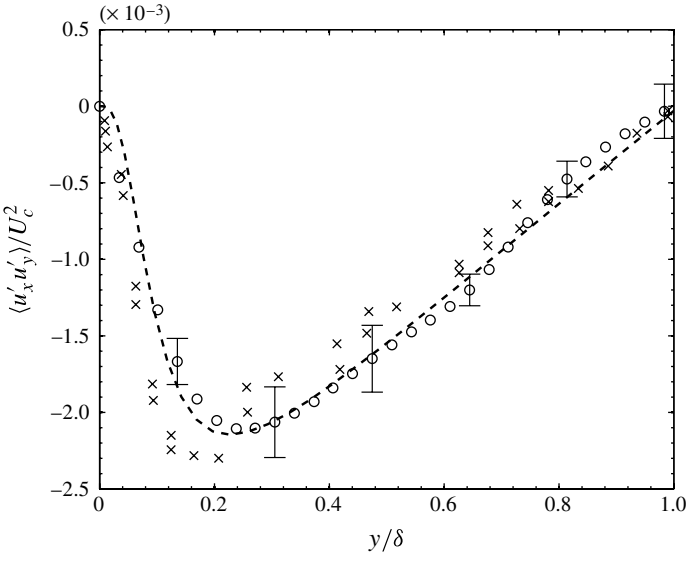

FIGURE 6. Second moment of gas-phase velocity fluctuation obtained from experiment and DNS. ∘, PIV, $Re_c = 2021.14$; - -, DNS, $Re_c = 2021.14$; ×, Niederschulte *et al.* (1990), $Re_c = 3221.5$.

for a higher solid volume faction for which particle–particle collision time is less than the particle relaxation time.

3.1. *Particle relaxation time less than particle–particle collision time*

The particles used for the experiment are 123.28 μm (number averaged mean diameter) glass spheres with volume fraction of 9.16×10^{-5}, which corresponds to a mass loading (the ratio of particle mass flux to fluid mass flux) of 19.4 %. To compare the experimental results with the FFS, we have performed FFS with using the same physical dimensions of the channel width and Reynolds number as used in the experiment. Periodic boundary conditions have been used in the streamwise and spanwise directions. The box size in the streamwise and spanwise directions is equal to the width of the channel, in order to reduce the number of particles simulated and the computation time.

In the direct simulations, the particle equation of motion can be described as

$$\frac{\mathrm{d}\boldsymbol{v}_i}{\mathrm{d}t} = \frac{\boldsymbol{u}_i\,(\boldsymbol{x}_{Pi}) - \boldsymbol{v}_i}{\tau_v} + \frac{1}{m_p}\sum_{i\neq j}\boldsymbol{C}_{ij} + \boldsymbol{g} \tag{3.1}$$

and

$$\frac{\mathrm{d}\boldsymbol{x}_i}{\mathrm{d}t} = \boldsymbol{v}_i, \tag{3.2}$$

where $\boldsymbol{u}_i(\boldsymbol{x}_{Pi})$ is the interpolated fluid velocity at the particle centre, $\boldsymbol{C}_{ij}$ is the force due to collisions and $\boldsymbol{g}$ is the gravitational acceleration. For the particle relaxation time (τ_v), we use an expression for (Coulson *et al.* 1998; Kumaran 2003) that incorporates the effect of particle inertia,

$$\tau_v = \frac{\rho_p d_p^2}{18\eta(1 + 0.15Re_p^{0.687})}, \tag{3.3}$$

where d_p is the particle diameter. The effect of inertia is incorporated because the particle Reynolds number, based on the maximum difference in the mean velocity between particle and air near the wall, is in the range 3–5 in the experiments.

In the fluctuating force model, the drag force on the particle is separated into two components, one due to the mean fluid velocity and the second due to the turbulent velocity fluctuations. The governing equation for the particle motion, (3.1), is approximated as

$$\frac{\mathrm{d}\boldsymbol{v}_i}{\mathrm{d}t} = \frac{\bar{\boldsymbol{u}}_i\,(\boldsymbol{x}_{Pi}) - \boldsymbol{v}_i}{\tau_v} + \frac{1}{m_p}\boldsymbol{F}_i(\boldsymbol{x}_{Pi}) + \frac{1}{m_p}\sum_{i\neq j}\boldsymbol{C}_{ij} + \boldsymbol{g}, \tag{3.4}$$

where $\bar{\boldsymbol{u}}_i(\boldsymbol{x}_p)$ is the mean velocity fluid velocity at the particle position, $\boldsymbol{F}_i(\boldsymbol{x}_p)$ is a stochastic force due to turbulent fluctuations. The correlation time of the turbulent fluctuations is small compared with the particle relaxation time, and the fluctuating force is modelled as a Gaussian random noise,

$$\langle F_i(\boldsymbol{x}, t)F_j(\boldsymbol{x}, t')\rangle = 2D_{ij}(\boldsymbol{x})\delta(t - t'), \tag{3.5}$$

where the position-dependent 'diffusion coefficient' D_{ij} is related to the autocorrelation function of the turbulent velocity fluctuations, as discussed in the Appendix of part 1 (Goswami & Kumaran 2011).

The polydispersity in the particle size distribution has been incorporated in the FFSs, since our studies have shown that polydispersity has a significant effect on the mean velocity and the root mean square of the fluctuating velocity in the simulations. When there is no polydispersity, the terminal velocities of all of the particles are

equal, and so collisions are induced only due to velocity fluctuations. When there is polydispersity, collisions could be induced by the difference in the terminal velocities of particles with different size, and this could increase the mean square of the fluctuating velocities of the particles. The polydispersity in the particle size distribution in the simulations is incorporated by matching the polydispersity in the relaxation time with that in the experiments, and then calculating the particle diameter from (3.3). The particles relaxation times are distributed, with equal probability, into 10 discrete values. The mean relaxation time in the experiments is 0.1257 s for particles with diameter 114.55 μm, while the standard deviation in the relaxation time is 0.0548 s. This same polydispersity is achieved by distributing the relaxation time in the simulations into 10 discrete equally spaced values in the range 0.0309–0.2206 s.

Another factor which we explore in the simulations is the coefficient of restitution in the particle–wall interactions, since it is found that this could have a significant effect on the concentration and the mean-square fluctuating velocity near the wall. Since data is not available for the exact nature of the particle–wall interactions, we use a collision model that has been previously used for shear flows (Kumaran 1997; Bose & Kumaran 2004), which contains a tangential and a normal coefficient of restitution for particle–wall collisions. When the normal coefficient of restitution is less than 1, the post-collisional cross-stream velocity is lower in magnitude than the pre-collisional velocity, resulting in the damping of cross-stream particle velocity fluctuations. When the tangential coefficient of restitution is less than 1, momentum is transferred from the particle to the wall in a collision, resulting in the slowing down of the particle in the streamwise direction. In our simulations, we have considered two different values of the tangential and normal coefficients of restitution, $e_t = 1.0$ and 0.7, and $e_n = 1.0$ and 0.7, in order to examine the effect of the restitution coefficients on the concentration and velocity profiles. Particle–particle collisions are elastic in all cases, since we expect the decrease in kinetic energy due to fluid drag to be larger than that due to inelastic collisions.

Finally, we briefly describe the procedure used for calculating the error bars in the experiments. All experimental results are based on averaging over a total of 3000 frames. To calculate the error bars in the experiments, we have considered 15 data subsets, consisting of 200 frames each. The averages have been calculated using the total 3000 frames, and standard deviation of that have been calculated based on the averages of the 15 subsets of 200 frames each.

3.1.1. *Gas-phase measurement*

The effect of particle loading on the gas phase has been examined, to determine the effect of particles on the turbulence intensity. In these measurements, the velocity vectors at different wall-normal positions are averaged over 3000 frames to obtain the mean and standard deviation of the different dynamical quantities. The mean velocity, mean square of the velocity fluctuations and the Reynolds stress for the unladen and particle-laden flows are compared in figures 7, 8 and 9 respectively. It is observed that the mean and the mean-square velocity for the unladen and particle-laden flows are nearly equal, to within the experimental resolution, indicating that the particles do not affect the gas-phase turbulence for the particle volume fraction considered here.

3.1.2. *Particle-phase measurement*

Figure 10 shows a comparison of the particle and air mean velocity profile obtained from the experiment and the FFSs. It is observed that in both cases, the particle mean velocity is higher than that of the air across the whole channel, but the mean slip velocity, which is the difference between the mean air velocity and that of the particle,

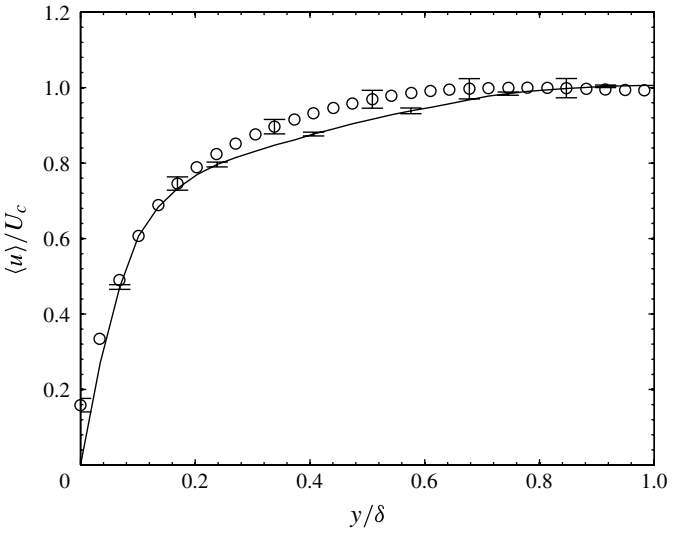

FIGURE 7. Mean gas velocity for particle-laden and unladen flows. (○), gas velocity of particle-laden flow; (—), gas velocity of unladen flow.

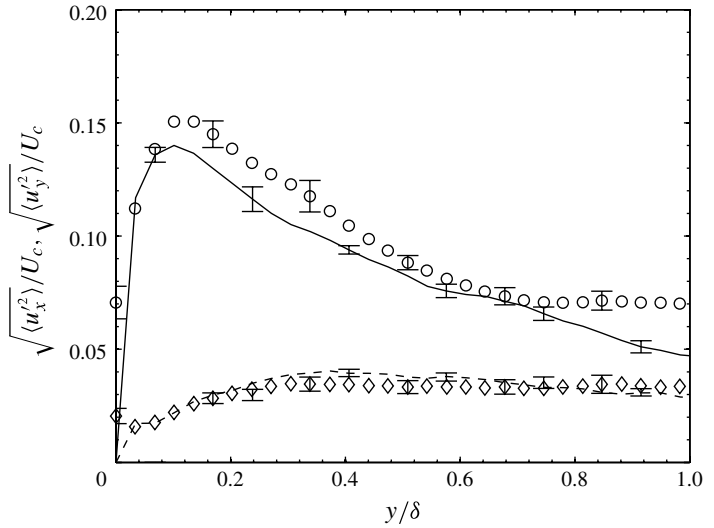

FIGURE 8. Experimental results of gas-phase turbulence intensities for particle-laden and unladen flows. (○), $\sqrt{\langle u_x'^2 \rangle}/U_c$, particle laden; (—), $\sqrt{\langle u_x'^2 \rangle}/U_c$, unladen; (◇), $\sqrt{\langle u_y'^2 \rangle}/U_c$, particle laden; (- -), $\sqrt{\langle u_y'^2 \rangle}/U_c$, unladen.

is higher near the wall and lower at the channel centre. To place the current results in context, we note the following results of previous studies. Khalitov & Longmire (2004) have reported that the particle mean velocity profile becomes flatter with increasing Stokes number, and they observed that particles with high Stokes number have a higher mean velocity than the gas at the wall, but a lower mean velocity at the centre.

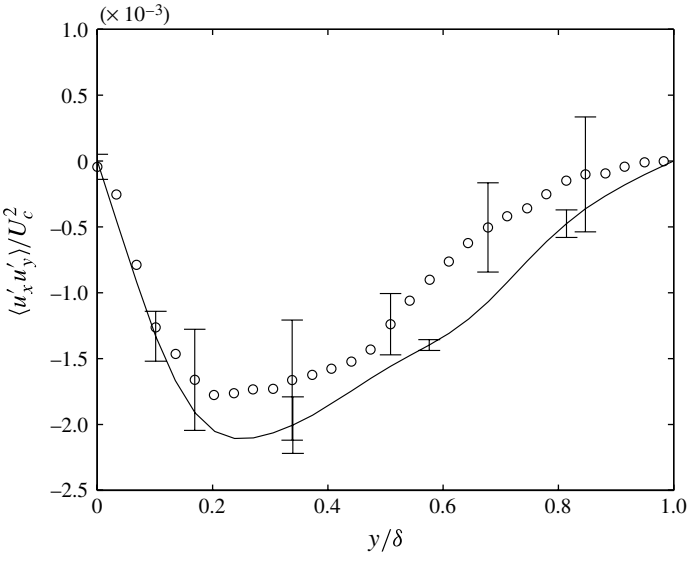

FIGURE 9. Second moment of the gas-phase velocity fluctuation for particle-laden and unladen flows. (○), particle laden; (—), unladen flow.

The difference could be because Khalitov & Longmire (2004) used a very narrow channel of width three times smaller than ours, and a Reynolds number (based on centre line velocity and half-width) of 4537, which is two times the Reynolds number used here. The Stokes number for their 20 μm particle is of the same magnitude as those for particles of mean diameter 123.28 μm in our experiment. Kulick *et al.* (1994) observed that 50 μm particles have a higher mean velocity than the gas near the wall, but a lower mean velocity at the centre, in their experiment of vertical channel flow for gas-phase Reynolds number of 13 800. They also found that the mean particle velocities are unaffected by the mass loading of the solid. Paris (2001) observed a flat velocity profile for the suspension of 150 μm particles, where particles at the centre of the channel move faster than the gas, while the particles at the wall move slower than the gas. In our experiment, the particle velocity is consistently higher than the gas velocity across the channel, and the velocity difference near the wall is ∼2.5 times higher than that at the channel centre. It is to be noted that for the vertical channel flow with the co-current motion of the gas and particle phases, the particle velocity averaged across the channel has to be higher than the gas velocity, so that the upward drag on the particle is balanced by the weight of the particle. Locally, the gas could move faster than the particles either due to insufficient development length, due to which the particle is not able to reach the terminal velocity, or due to motion of particles across the channel from low mean velocity region to the higher mean velocity region, induced by particle–particle and particle–wall collisions, or due to the transverse velocity fluctuation of the gas phase. Paris (2001) used a development length of 5.2 m which provides a particle residence time, which is four times the particle relaxation time, and reported that particle migration is the main contributor to the flattening of the mean particle velocity. This occurs if the transverse distance travelled by the particles, over a time scale comparable to the relaxation time, is comparable to the channel width. In our experiments, since the gas-phase Reynolds number is much smaller than the other studies reported above, the particle fluctuating

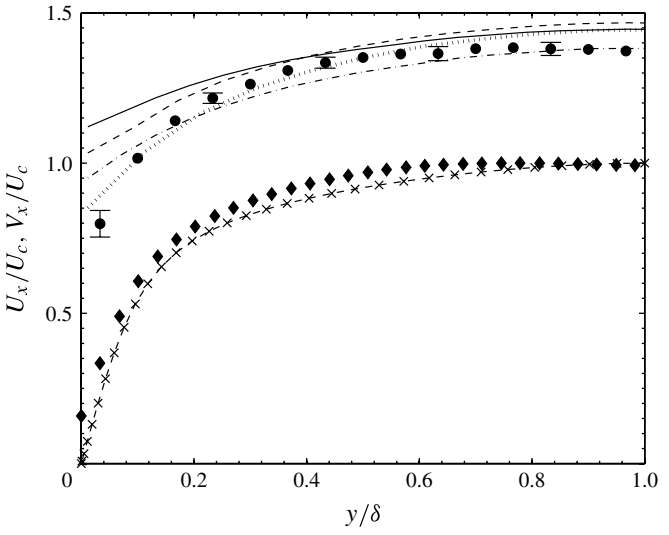

FIGURE 10. Mean streamwise velocity of the particle at different wall-normal positions, from experiment and FFS. (●), mean particle velocity (V_x), experiment; (⧫), mean air velocity (U_x), experiment; (−×−), U_x, FFS; (—), V_x/U_c, $e_n = e_t = 1.0$, FFS; (− · −), FFS, V_x/U_c, $e_n = 1.0$, $e_t = 0.7$, FFS; (- -), V_x/U_c, $e_n = 0.7$, $e_t = 1.0$, FFS; (· · ·), V_x/U_c, $e_n = 0.7$, $e_t = 0.7$, FFS.

velocity in the transverse direction is much smaller. This leads to less cross-stream motion of the particles, and the particles at the centre of the channel also move faster than the air phase.

Near the wall, there is some dependence of the mean velocity on the tangential coefficient of restitution for particle–wall collision, as shown in figure 10. As the tangential coefficient of restitution is decreased, the mean velocity at the wall decreases due to the transmission of momentum from the particle to the wall in particle–wall collisions. A decrease in the normal coefficient of restitution does not alter the mean velocity very much, since it affects only the wall-normal component of the particle velocity. A comparison with experimental results shows that an elastic particle–wall collision law ($e_t = 1.0$) overestimates the mean velocity at the wall, whereas the simulations for $e_t = 0.7$ is in excellent numerical agreement with experiments. However, there is very good agreement between simulations and experiments away from the wall. This indicates that the FFSs can quantitatively capture the mean velocity profile of the particles in the bulk of the flow, but it is necessary to incorporate the correct collision law for particle–wall collisions in order to quantitatively predict the mean velocity near the wall.

Next, we turn to the intensity of particle velocity fluctuations. Figure 11 shows both the streamwise and wall-normal particle velocity fluctuations obtained from experiments and from FFSs. Both of the components of root-mean-square velocity fluctuations have been non-dimensionalized with the maximum centre-line particle velocity. Figure 11 shows that streamwise component of particle velocity fluctuations is higher than the wall-normal component. This is due to two reasons. One reason is that the fluid velocity fluctuation is higher in the streamwise direction, and this leads to a higher fluctuating force on the particles in the streamwise direction. Second, there is a cross-stream motion of the particle from the wall to the centre and vice versa.

Figures 11 and 8 show that the intensity of particle velocity fluctuation is higher than the fluid velocity fluctuation throughout the channel, even though the particle Stokes number based on the fluid integral time scale is $O(1)$, due to the polydispersity, and collisions between different-sized particles. Figure 11 also shows that the damping of the particle velocity due to particle–wall collisions has a significant effect on the mean square of the fluctuating velocity. Simulations carried out with inelastic particle–wall collisions overestimate the fluctuating velocity in the streamwise direction. As expected, a decrease in the normal coefficient of restitution decreases the wall-normal fluctuating velocity. With the exception of the near-wall region, the streamwise and the wall-normal mean-square velocities from the simulations are in quantitative agreement with experiments for $e_n = 1.0, e_t = 1.0$. Near the wall, the experiments show a systematic decrease in the cross-stream mean square of the fluctuating velocity, which is not captured by the simulations. However, a decrease in the coefficient of restitution does decrease the cross-stream mean-square velocity to the value near the wall. Figure 12 shows a comparison of the second moment $\langle v_x' v_y' \rangle$ of the particle fluctuating velocity. There are large error bars in the measurement of $\langle v_x' v_y' \rangle$, because the magnitude of this second moment is much smaller than the mean-square velocities in the streamwise and wall-normal conditions (figure 11). In the simulations, the effect of inelasticity of particle–wall collisions on $\langle v_x' v_y' \rangle$ is significantly larger than that on the streamwise and wall-normal mean-square velocities. The simulation results for elastic particle–wall collisions are not in agreement with the experimental results, but quantitative agreement (subject to experimental error bars) is obtained when the normal coefficient of restitution is set equal to 0.7.

The results obtained here are also broadly in agreement with previous studies. Khalitov & Longmire (2004) have found a higher streamwise velocity fluctuation and lower spanwise velocity fluctuation compared with the fluid velocity fluctuation; they have conducted experiments in the streamwise–spanwise plane at different wall-normal positions, and did not measure the wall-normal velocity fluctuation. Paris (2001) observed higher streamwise and wall-normal particle velocity fluctuations than that of the gas phase throughout the channel, with the exception of the near-wall region.

Figure 13 shows the variation of particle concentration, scaled by the average concentration across the channel. The concentration profile in the FFSs is almost independent of position. In the simulations, there is a slight increase in the concentration at the walls when the coefficient of restitution is decreased, but the magnitude of the increase is small for $e_t = 0.7$. There is a somewhat larger variation in the concentration obtained from experiments, but this is subject to relatively large error bars, indicating the presence of concentration inhomogeneities across the channel. Surprisingly, the experiments show a decrease in the concentration at the wall, in contrast to a naive expectation that the concentration should increase if the particle–wall collisions are inelastic. The low concentration may originate from the feeding of the particle. Since we are using the vibratory hopper as a feeder, due to the high friction of the particle with the wall of the hopper there is a possibility of the low feed rate of the particle at the near-wall region. Khalitov & Longmire (2004) have also reported an increase in the solid concentration as the centre of the channel is approached for a wide range of particle diameters from 20 μm to 160 μm.

We have computed the particle fluctuating velocity distribution function at two locations, the first is in the centre of width equal to 10 % of the total width, and the other is the region near the wall. These two positions are shown as A and C in figure 5. To obtain the fluctuating velocity, the local time average velocity is subtracted from the instantaneous particle velocity. While plotting the distribution function, we

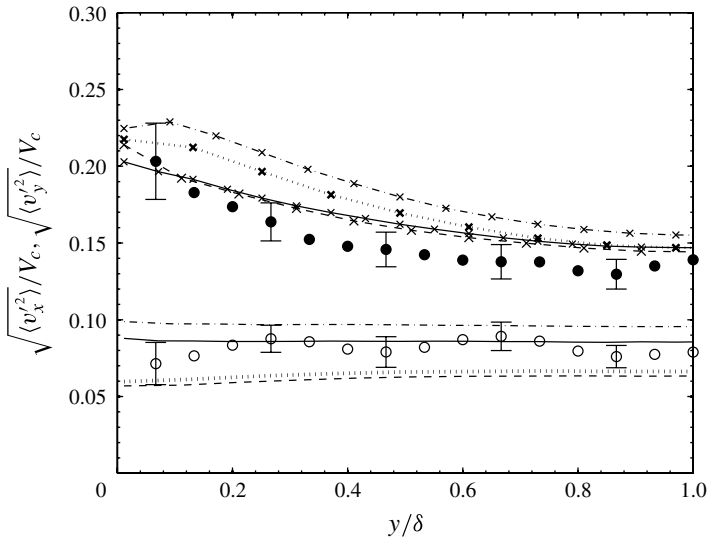

FIGURE 11. Intensity of particle-phase velocity fluctuation at different wall-normal positions. (•), $\sqrt{\langle v_x'^2\rangle}/V_c$, experiment; (○), $\sqrt{\langle v_y'^2\rangle}/V_c$, experiment; (—×), $\sqrt{\langle v_x'^2\rangle}/V_c$, $e_n = e_t = 1.0$, FFS; (− · ×), $\sqrt{\langle v_x'^2\rangle}/V_c$, $e_n = 1.0$, $e_t = 0.7$, FFS; (- - ×), $\sqrt{\langle v_x'^2\rangle}/V_c$, $e_n = 0.7$, $e_t = 1.0$, FFS; (· · · ×), $\sqrt{\langle v_x'^2\rangle}/V_c$, $e_n = 0.7$, $e_t = 0.7$, FFS; (—), $\sqrt{\langle v_y'^2\rangle}/V_c$, $e_n = e_t = 1.0$, FFS; (−·), $\sqrt{\langle v_y'^2\rangle}/V_c$, $e_n = 1.0$, $e_t = 0.7$, FFS; (- -), $\sqrt{\langle v_y'^2\rangle}/V_c$, $e_n = 0.7$, $e_t = 1.0$, FFS; (· · ·), $\sqrt{\langle v_y'^2\rangle}/V_c$, $e_n = 0.7$, $e_t = 0.7$, FFS.

have normalized the fluctuating velocity by local standard deviation of the particle velocity. This enables us to examine whether the form of the velocity distribution function in experiments can be correctly captured from simulations. The standard deviations have been calculated based on 3000 samples. Figure 14(*a*) shows the comparison in probability density function (p.d.f.) of the streamwise particle velocity distribution computed from the central region of the channel. From figure 14(*a*) it is observed that there is a negative skewness in the distribution function for the streamwise fluctuating velocity in both simulations and experiments. However, there is some difference in the detailed shape of the distribution function. The distribution function from FFS shows an asymmetric bi-modal type distribution with a larger peak at positive velocity fluctuation, and the lower peak at the negative velocity fluctuation. From the experimental results we are not able to distinguish a peak for negative velocity. The bi-modal shape of the distribution function from FFS also depends on the wall–particle coefficient of restitution used in the simulation; in particular, the second peak is less pronounced when the wall-normal coefficient of restitution is 0.7. It is also observed that presence of polydispersity plays an important role in the shape of the distribution function. We have run some simulations using monodispersed particles with relaxation time equal to the mean relaxation time of the polydispersed particles as shown in figure 14(*b*). Although this result shows skewness in the distribution function, the shape is not bi-modal for the range of coefficient of restitution studied. Therefore,

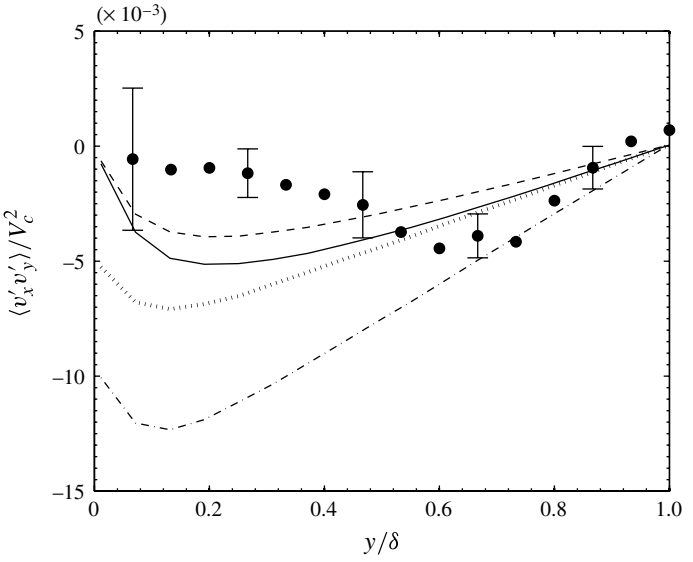

FIGURE 12. Second moment of the particle velocity fluctuation ($\langle v_x' v_y' \rangle$) at different wall-normal positions. (•), experiment; (—) $e_n = e_t = 1.0$, FFS; (– · –), $e_n = 1.0$, $e_t = 0.7$, FFS; (- -), $e_n = 0.7$, $e_t = 1.0$, FFS; (· · ·), $e_n = 0.7$, $e_t = 0.7$, FFS.

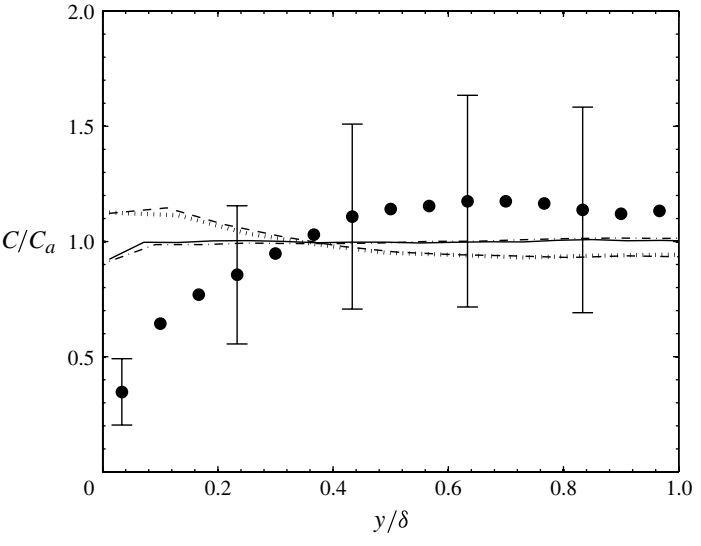

FIGURE 13. Variation of particle concentration across the channel. (•), experiment; (—), $e_n = e_t = 1.0$, FFS; (– · –), $e_n = 1.0$, $e_t = 0.7$, FFS; (- -), $e_n = 0.7$, $e_t = 1.0$, FFS; (· · ·), $e_n = 0.7$, $e_t = 0.7$, FFS.

the sensitivity of the shape of the distribution function to polydispersity at the centre is evident from figure 14(*a*,*b*).

In figure 15, the p.d.f. of the wall-normal particle velocity fluctuations shows a quantitative agreement with the result obtained from FFS, even up to a very low value

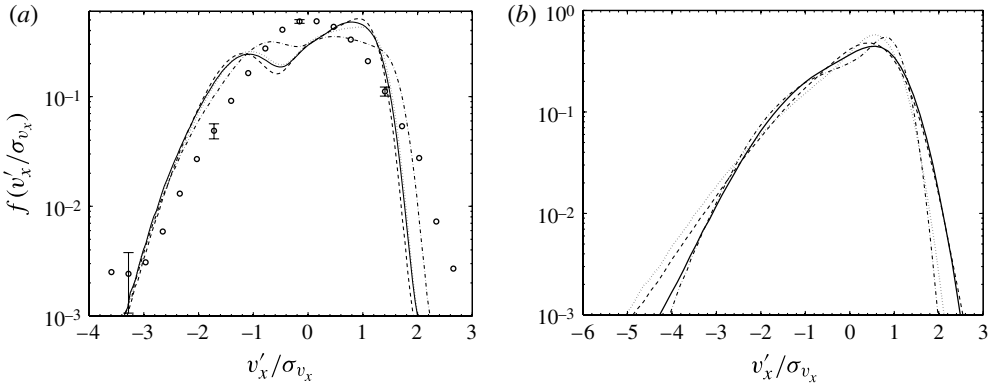

FIGURE 14. Distribution of the streamwise component of the particle velocity fluctuation at the centre of the channel for (*a*) polydispersed particles and (*b*) monodispersed particles. ∘, experiment; (—), $e_n = e_t = 1.0$, FFS; (– · –), $e_n = 1.0$, $e_t = 0.7$, FFS; (- -), $e_n = 0.7$, $e_t = 1.0$, FFS; (· · ·), $e_n = 0.7$, $e_t = 0.7$, FFS. For monodispersed particles the relaxation time is equal to the mean relaxation time of the polydispersed particles.

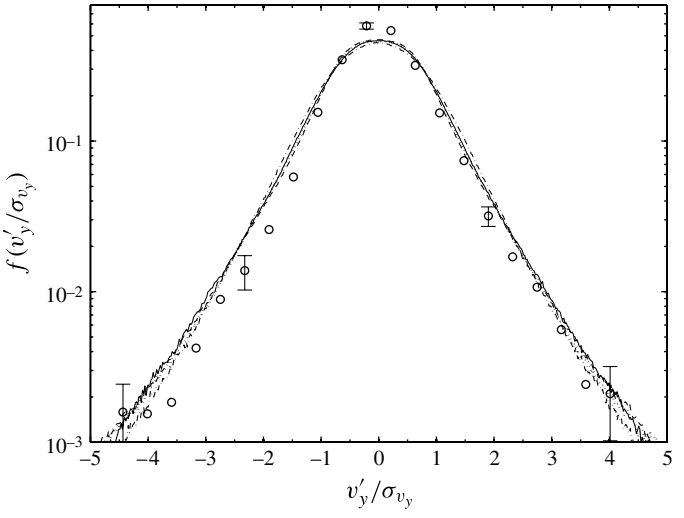

FIGURE 15. Distribution of the wall-normal component of the particle velocity fluctuation at the centre of the channel. ∘, experiment; (—), $e_n = e_t = 1.0$, FFS; (– · –), $e_n = 1.0$, $e_t = 0.7$, FFS; (- -), $e_n = 0.7$, $e_t = 1.0$, FFS; (· · ·), $e_n = 0.7$, $e_t = 0.7$, FFS.

of the distribution function of 10^{-3}. The results from the FFSs are relatively insensitive to the coefficient of restitution for wall–particle collisions.

Figures 16(*a*) and 17 show the p.d.f. of streamwise and wall-normal velocity fluctuation near the wall ($y/\delta = 0.05$–0.15). Once again, the distribution of the streamwise fluctuating velocity has a negative skewness in both simulations and experiments. In the simulations the form of the distribution function depends on the wall–particle coefficient of restitution. The distribution function has one peak for $e_n = 1.0$, and two peaks for $e_n = 0.7$. The results for $e_n = 1.0$ and $e_t = 0.7$ are in good quantitative agreement with experiments, subject to the experimental error bars.

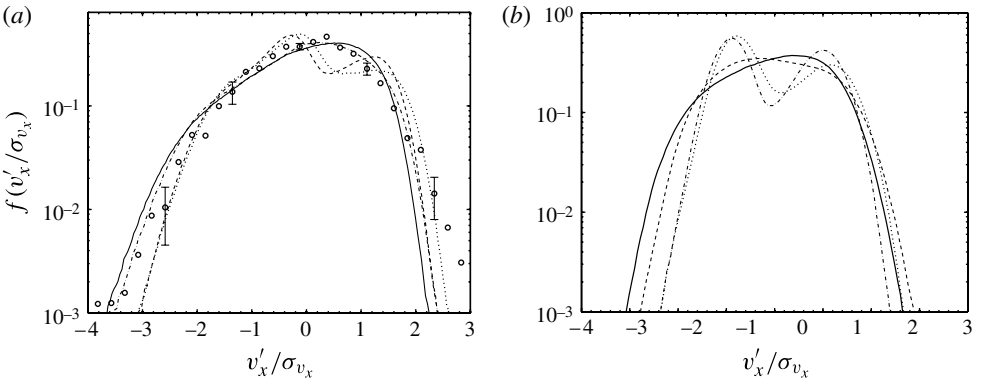

FIGURE 16. Distribution of the streamwise component of the particle velocity fluctuation at the near-wall region of the channel for (*a*) polydispersed particles and (*b*) monodispersed particles. ∘, experiment; (—), FFS, $e_n = e_t = 1.0$; (— · —), FFS, $e_n = 1.0$, $e_t = 0.7$; (- -), FFS, $e_n = 0.7$, $e_t = 1.0$; (· · ·), FFS, $e_n = 0.7$, $e_t = 0.7$. For monodispersed particles the relaxation time is equal to the mean relaxation time of the polydispersed particles.

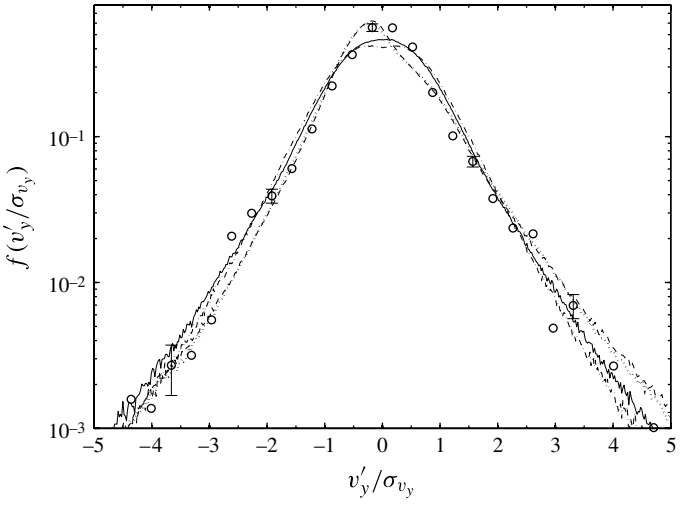

FIGURE 17. Distribution of the wall-normal component of the particle velocity fluctuation at the near-wall region of the channel. ∘, experiment; (—), FFS, $e_n = e_t = 1.0$; (— · —), FFS, $e_n = 1.0$, $e_t = 0.7$; (- -), FFS, $e_n = 0.7$, $e_t = 1.0$; (· · ·), FFS, $e_n = 0.7$, $e_t = 0.7$.

The sensitivity of the shape of the distribution function to coefficient of restitution in the near-wall region can be seen in figure 16(*b*). Therefore, there appears to be many factors which affect the nature of the distribution, including the polydispersity and the coefficient of restitution, and further work is required to separate out all of the effects. However, bi-modal distributions have been observed before in flows of granular materials as discussed below.

Bi-modal distributions have been observed previously in granular shear flows bounded by solid walls, where the a wall-collision model with normal and tangential coefficients of restitution is used (Kumaran 1997; Bose & Kumaran 2004). In this model, the tangential component of the post-collision particle fluctuating

velocity $v_x'^*$ is related to the pre-collisional fluctuating velocity by v_x' by the relation $v_x'^* = e_t v_x' - (1 - e_t)V_w$, where V_w is the mean particle-phase velocity at the wall. As shown in Goswami & Kumaran (2011), there is usually slip at the wall, so the mean particle-phase velocity is non-zero. The wall collisions in the tangential restitution model reduce the tangential velocity by a finite amount $(1 - e_t)V_w$. This results in a bi-modal distribution, with one peak corresponding to the most probable pre-collisional velocity, and the second to the post-collisional velocity corresponding to the most probable pre-collisional velocity. Previous studies have also observed this feature in a more detailed particle model which incorporates the rotational degrees of freedom (Kumaran 2005, 2006). This explains the bi-modal nature of the distribution for rough walls, but the experimental distribution function appears smooth, indicating that further refinements are necessary in the particle–wall distribution.

Figure 17 shows that experimentally determined p.d.f. for wall-normal component of particle velocity fluctuation is also in quantitative agreement with the FFS, and the distribution of the wall-normal fluctuating velocities is insensitive to the particle–wall coefficients of restitution.

3.2. *Collision time less than the particle relaxation time*

In this section we discuss the particle- and gas-phase statistics for the regime when the particle–particle collision time is less than the viscous relaxation time of the particle. For this regime the solid volume fraction is 8.2×10^{-4}, and mass loading is $\sim$1.7 which is one order of magnitude higher than the previous regime, so that collision time also decreases by an order of magnitude for the same volumetric gas flow rate. Since there is unwanted multiple light scattering at higher volume fraction, the aperture is reduced in such a way that the f-number ($F\#$) of the lens becomes 4.0 instead of 2.8 in the previous case. Owing to the decrease in the signal-to-noise ratio, it is necessary to reduce the threshold limit in intensity for the separation of solid particle and tracer. Using this, we process the raw multiphase images to obtain the velocity fields.

3.2.1. *Gas-phase measurement*

First we examine the effect of particles on the gas-phase statistics. In these measurements, the velocity vectors at different wall-normal positions are averaged over 1000 frames to get the mean and standard deviation of the different dynamical quantities. The mean velocity, mean square of the velocity fluctuations and the Reynolds stress for the unladen and particle-laden flows are shown in figures 18, 19 and 20, respectively. Here, the air velocities are normalized by the centre-line air velocity. The centre-line gas velocity in the presence of the particles is adjusted, by changing the pressure drop, so that it becomes equal to that for the unladen flow. As a result, the Reynolds number based on the channel centre-line air velocity is the same in both the unladen and particle-laden flows. It is observed that the mean velocity profile for the unladen and particle-laden flows are nearly equal except very near the wall, indicating that the particle loading is not significantly changing the gas velocity profile except very near the wall.

Figure 19 shows the turbulent intensity in the presence and in the absence of the particles. It is found that in presence of particles, the turbulent intensity is about an order of magnitude higher than that for the unladen flow. In this context it should be mentioned that Li & McLaughlin (2001) have observed a decrease in turbulent intensity in their simulation for the solid loading, which is approximately the same as the present case, although their channel width was $\sim$5-fold less. Recently, Tanaka & Eaton (2008) have reviewed the available experimental data and separated the

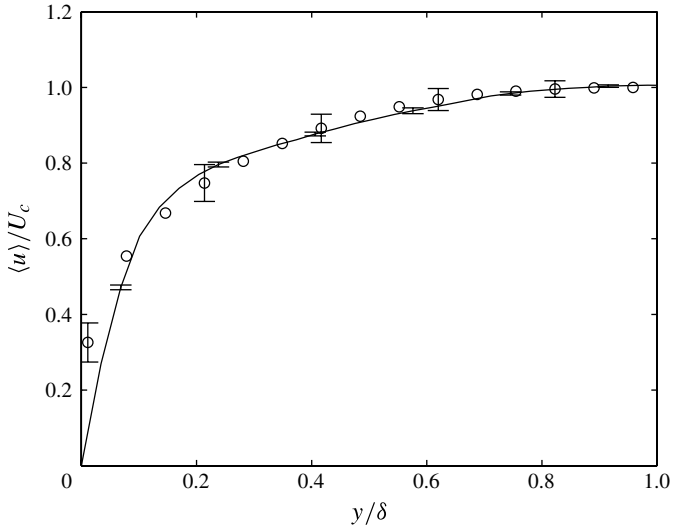

FIGURE 18. Mean gas velocity for particle-laden and unladen flows. (○), gas velocity of particle-laden flow; (—), gas velocity of unladen flow.

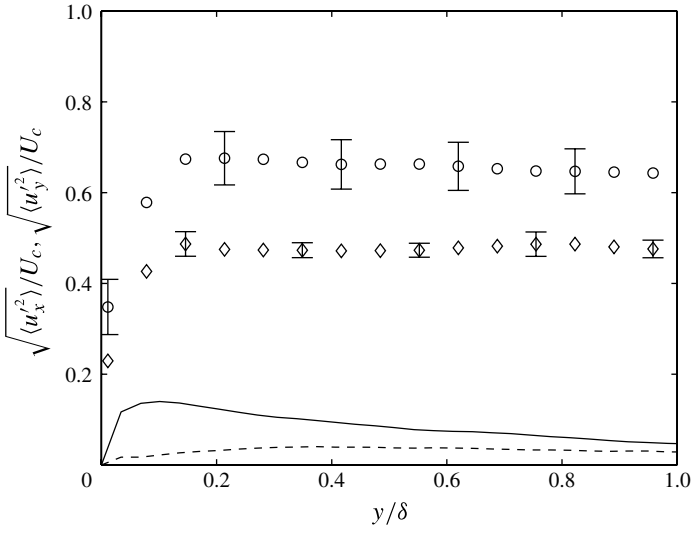

FIGURE 19. Experimental results of gas-phase turbulence intensities for particle-laden and unladen flows. (○), $\sqrt{\langle u_x'^2 \rangle}/U_c$, particle laden; (—) $\sqrt{\langle u_x'^2 \rangle}/U_c$, unladen; (◇), $\sqrt{\langle u_y'^2 \rangle}/U_c$, particle laden; (- -), $\sqrt{\langle u_y'^2 \rangle}/U_c$, unladen.

regime of turbulent kinetic energy augmentation and attenuation based on the Reynolds number and particle momentum number. In their map (figure 1*b* of Tanaka & Eaton 2008) the present experiment (with particle momentum number approximately equal to 10) falls on the augmentation side, although they have not mentioned the effect of particle loading. The modified turbulent intensities, calculated for the particle–laden channel flow, are now used in our FFS simulations to make a comparison with

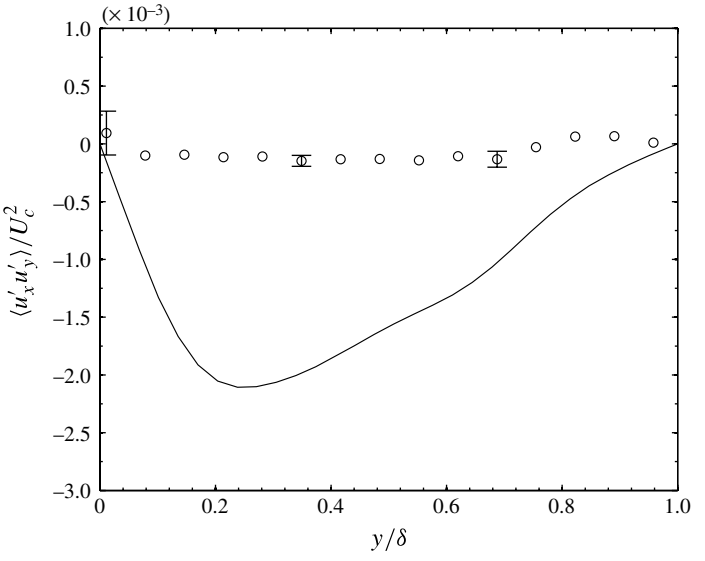

FIGURE 20. Second moment of the gas-phase velocity fluctuation for particle-laden and unladen flows. (○), particle laden; (—), unladen flow.

experiments. The diffusion coefficient in the FFS is the product of the fluid mean-square velocity and the fluid integral time. We do not have direct access to the fluid integral time for the particle-laden flow, since our simulations have only one-way coupling. Therefore, in the FFS, we have considered the modified turbulent diffusivity calculated based on the modified turbulent intensity from the experiments, although we have assumed that the fluid integral time scale is not affected due to the presence of particle. Then the particle statistics obtained from the FFS has been compared with the experimental observations.

3.2.2. *Particle-phase measurement*

Figure 21 shows the particle mean velocity, normalized by the centre-line air velocity, obtained from experiments and FFS. It is observed that the gas velocity is higher than the particle phase at the centre of the channel. This is in contrast to the low loading regime studied in the previous section, where the collision time is less than the viscous relaxation time of the particle. It is observed that the gas-phase velocity is higher than the particle-phase velocity at the centre of the channel; a similar result has also been reported by Li & McLaughlin (2001). We have compared the experimental result with FFS using different values of tangential coefficient of restitution (e_t) although the normal coefficient of restitution (e_n) is considered to be 1 for simplicity.

Figure 21 shows the particle mean velocity predicted by FFS is ∼1.4 times higher than the experimentally determined values when the tangential coefficient of restitution (e_t) is 1. However, for $e_t = 0.7$ the particle velocity is within 10 % of the experimentally determined mean velocity near the centre of the channel, although FFS predicts a higher velocity near the wall. This indicates that there is significant transmission of streamwise momentum from the particle to the wall in particle–wall collisions, and this has to be incorporated to make accurate predictions of the particle velocity profile.

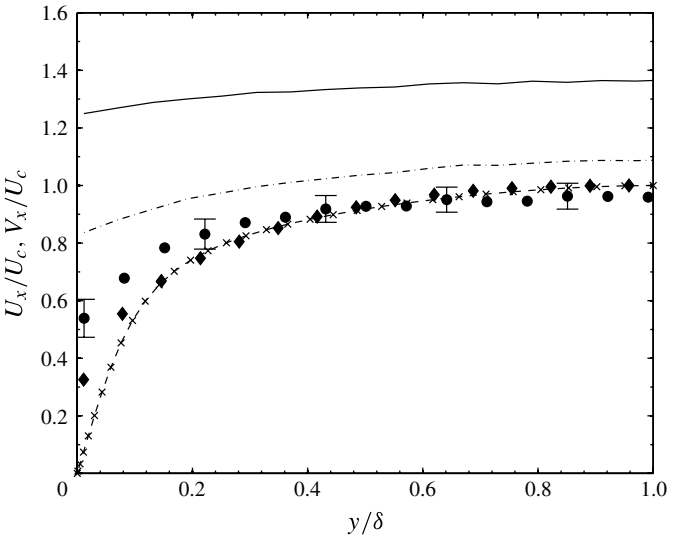

FIGURE 21. Mean streamwise velocity of the particle at different wall-normal positions, from experiment and FFS. (●), mean particle velocity (V_x), experiment; (⧫), mean air velocity (U_x), experiment; (− × −), U_x, FFS; (—), V_x, $e_n = e_t = 1.0$; (− · −), V_x, $e_n = 1.0$, $e_t = 0.7$.

Figure 22 shows the intensity of the particle velocity fluctuation in the streamwise and cross-stream direction at different wall-normal positions. It is found that changing the tangential coefficient of restitution has opposite effects on the streamwise and cross-stream velocity fluctuations. FFS over-predicts the wall-normal particle velocity fluctuation by ∼18 % when $e_t = 1.0$, but in that case streamwise particle velocity fluctuation is under-predicted by 30 %. In contrast, for $e_t = 0.7$, FFS over-predicts the wall-normal fluctuation by 40 % but streamwise particle velocity fluctuation is well predicted within 10 %. Figure 23 shows the second moment ($\langle v_x' v_y' \rangle$) of the particle velocity fluctuation along the wall-normal position in the channel. It is found that as the tangential coefficient of restitution decreases the FFS results deviates more strongly from the experimental result.

Figure 24 shows the variation of particle concentration, scaled by the average concentration across the channel. The concentration profile in the FFSs is almost independent of position and the tangential coefficient of restitution. There is a larger variation in the concentration obtained from experiments, indicating the presence of concentration inhomogeneities across the channel. Surprisingly, the experiments show a decrease in the concentration at the wall, in contrast to the higher concentration expected if the particle–wall collisions are inelastic. The low concentration may originate from the feeding of the particles, as discussed in § 3.1.2.

4. Conclusions

An important issue in the experiments is the polydispersity in the particle size distribution. Although care was taken here to reduce the polydispersity to the largest extent possible, the experimental samples still contained a polydispersity of ∼20 %. This polydispersity was also incorporated into the FFSs. We have also carried out

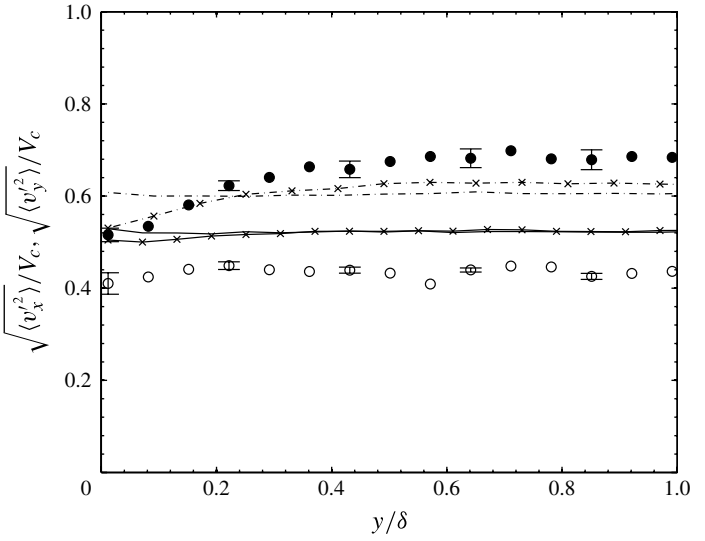

FIGURE 22. Intensity of particle-phase velocity fluctuation at different wall-normal positions. Filled symbols are for experiments and open symbols are for FFSs. (•), $\sqrt{\langle v_x'^2\rangle}/V_c$, experiment; (○), $\sqrt{\langle v_y'^2\rangle}/V_c$, experiment; (—×), $\sqrt{\langle v_x'^2\rangle}/V_c$, $e_n = e_t = 1.0$, FFS; (− · ×), $\sqrt{\langle v_x'^2\rangle}/V_c$, $e_n = 1.0$, $e_t = 0.7$, FFS; (—), $\sqrt{\langle v_y'^2\rangle}/V_c$, $e_n = e_t = 1.0$, FFS; (− · −), $\sqrt{\langle v_y'^2\rangle}/V_c$, $e_n = 1.0$, $e_t = 0.7$, FFS.

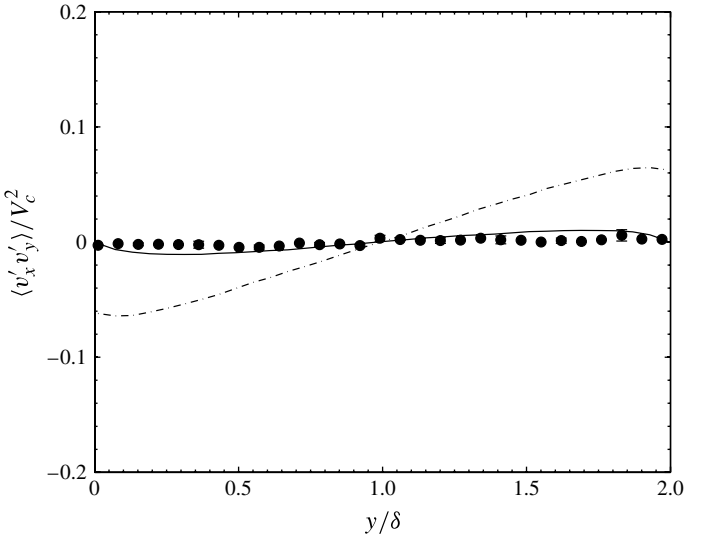

FIGURE 23. Second moment of the particle velocity fluctuation ($\langle v_x' v_y'\rangle$) at different wall-normal positions. Filled symbols are for experiment and the open symbols are for FFSs. (•), experiment; (—) $e_n = e_t = 1.0$, FFS; (− · −) $e_n = 1$, $e_t = 0.7$, FFS.

some simulation runs which did not include the polydispersity, and have found that the polydispersity has a significant effect on the mean square of the particle velocity fluctuations.

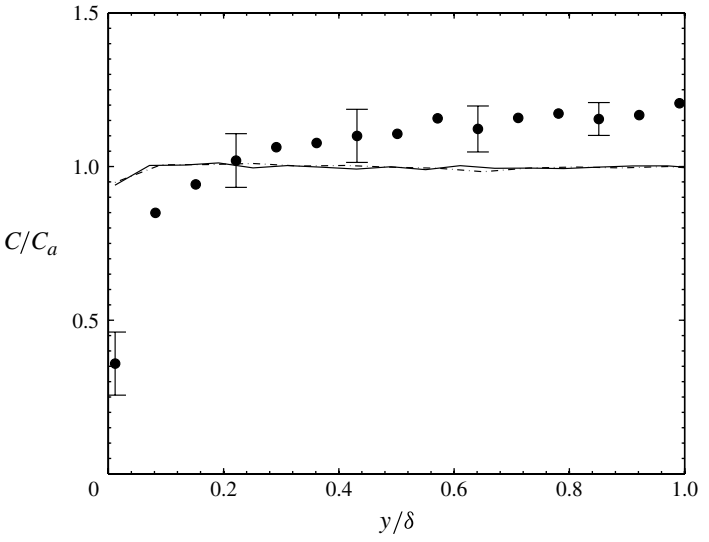

FIGURE 24. Variation of particle concentration across the channel. Filled symbols are for experiment and the open symbols are for FFSs. (•), experiment; (—), $e_n = e_t = 1.0$, FFS; $(- \cdot -)$, $e_n = 1.0$, $e_t = 0.7$, FFS.

For experiments carried out at a low volume fraction of 9.15×10^{-5} where the viscous relaxation time is small compared with the time between collisions, it is found that the gas-phase turbulence is not significantly modified by the presence of particles. Owing to this, quantitative agreement is obtained between the results of experiments and FFSs for the mean velocity and the root mean square of the fluctuating velocity. It is found that there is some variation in the particle mean velocity very close to the wall depending on the wall-collision model used in the simulations, and agreement with experiments is obtained only when the tangential wall–particle coefficient of restitution is 0.7. However, the mean particle velocity is in quantitative agreement for locations more than 10 wall units from the wall of the channel. There was also some difference in the particle concentration across the channel in the experiments, which is in contrast to the near constant across the channel in simulations. Quantitative agreement is also found for the root mean square of the particle fluctuating velocities in the streamwise and wall-normal directions. There is some discrepancy between simulations and experiments for the second moment $\langle v_x' v_y' \rangle$. However, it should be noted that $\langle v_x' v_y' \rangle$ is small, $\sim 10^{-2}$ times the root-mean-square velocity in the flow direction, and so the error bars in this measurement are relatively large. The particle velocity distributions are compared both at the centre of the channel and near the wall. The shape of the distribution function near the wall, obtained in experiments is accurately predicted by the simulations. At the centre, there is a small discrepancy between simulations and experiment for the distribution of the fluctuating velocity in the flow direction. Whereas the simulations predicted a bi-modal distribution, only a single maximum was observed in the experiments, although both distributions have a skewness towards negative fluctuating velocities. The distribution function for the velocity in the gradient direction is well predicted by the simulations.

At a much higher particle volume fraction where the particle loading is 1.7, it is found that the gas-phase turbulent intensity becomes more than an order of magnitude higher than the unladen case. Therefore, it is necessary to incorporate the modified

fluid-phase intensity in the FFSs; if the turbulence intensity is not modified, we find that the FFS simulations predict mean-square velocities that are about an order of magnitude smaller than those in experiments. The modified diffusion coefficients in the FFS involve the mean square of the fluid velocity fluctuations, as well as the integral time scale for the fluid. The former were taken directly from experiments, but we did not have access to the latter, and so we assumed that the integral time scales were the same as with the unladen flow. Future work is required to improve this approximation. Even with this assumption, it is found that the deviation in mean velocity and the mean square of the fluctuating velocities of the particle are within ∼20–30 % of experimental results only when the tangential particle restitution coefficient used is in the range 0.7–1.0.

Thus, our simulations show that there is good agreement between the FFSs and experiments at low loading, where the viscous relaxation time is small compared with the collision time, provided that the polydispersity in the particle size distribution is incorporated in the simulations. At high loading, where the collision time is small compared with the viscous relaxation time, we find that there is significant turbulent modification due to the particles. Despite this, the results of the FFSs are found to differ by ∼20–30 % of the experimental results, provided that the diffusion coefficient is altered to incorporate the turbulence modification.

There are some important implications of our comparison of simulations and experiments. At the start of the introduction, we had highlighted the importance of the particle-level relative velocity between the fluid and particles for the heat and mass transport rates, and thereby for the design of reactors or combustors. At the highest mass loading of 1.7 that we have studied, we obtain an agreement between experimental and simulation results, which differs by a maximum of 30 % for the mean and root mean square of the fluctuating velocities, obtained from simulations and experiment, provided that the polydispersity in the particle phase and the turbulence modification are incorporated. It should be noted that there are no fitting parameters in the model. While the agreement is not perfect, it could serve as an important first step in incorporating particle-level fluctuations into design considerations. We should note that we have considered a mass loading that is larger than that typically studied using velocimetry (Paris 2001; Khalitov & Longmire 2003). The results are significantly better at the lower volume fraction, where turbulence modification is not significant, and quantitative agreement is obtained. Even here, our study underlines the importance of correctly incorporating polydispersity and particle–wall contact laws.

The authors would like to thank the Department of Science and Technology, Government of India for financial support and Mr M. Rao, support staff of the Department of Chemical Engineering, Indian Institute of Science for his contribution in setting up experimental facilities. We also acknowledge CSIR C-MMACS computational facilities for running some simulations.

REFERENCES

BAGCHI, P. & BALACHANDAR, S. 2003 Effect of turbulence on the drag and lift of a particle. *Phys. Fluids* **15**, 3496–3513.

BALACHANDAR, S. & EATON, J. K. 2010 Turbulent dispersed multiphase flow. *Annu. Rev. Fluid Mech.* **42**, 111–133.

BOSE, M. & KUMARAN, V. 2004 Velocity distribution for a two-dimensional sheared granular flow. *Phys. Rev.* E **69**, 061301.

BURTON, T. M. & EATON, J. K. 2005 Fully resolved simulation of particle-turbulence interaction. *J. Fluid Mech.* **545**, 67–111.

COULSON, J. M., RICHARDSON, J. F., BACKHURST, J. R. & HARKER, J. H. 1998 *Chemical Engineering*. Asian Books Private Limited.

ELGHOBASHI, S. & TRUESDELL, G. C. 1993 On the two-way interaction between homogeneous turbulence and the dispersed solid particles 1: turbulence modification. *Phys. Fluids* A **5**, 1790.

FESSLER, J. R., KULICK, J. D. & EATON, J. K. 1994 Preferential concentration of heavy particles in a turbulent channel flow. *Phys. Fluids* **6**, 3742–3749.

GORE, R. A. & CROWE, C. T. 1989 Effect of particle size on modulating turbulent intensity. *Intl J. Multiphase Flow* **15**, 279.

GOSWAMI, P. S. 2009 Particle dynamics in a turbulent particle–gas suspension at high Stokes number. PhD thesis, Indian Institute of Science, India.

GOSWAMI, P. S. & KUMARAN, V. 2010*a* Particle dynamics in a turbulent particle–gas suspension at high Stokes number. Part 1. Velocity and acceleration distributions. *J. Fluid Mech.* **646**, 59–90.

GOSWAMI, P. S. & KUMARAN, V. 2010*b* Particle dynamics in a turbulent particle–gas suspension at high Stokes number. Part 2. The fluctuating force model. *J. Fluid Mech.* **646**, 91–125.

GOSWAMI, P. S. & KUMARAN, V. 2011 Particle dynamics in the channel flow of a turbulent particle–gas suspension at high Stokes number. Part 1. DNS and fluctuating force model. *J. Fluid Mech.* **687**, 1–40.

HETSRONI, G. 1989 Particle–turbulence interaction. *Intl J. Multiphase Flow* **15**, 735.

HWANG, W. & EATON, J. K. 2006 Homogeneous and isotropic turbulence modulation by small heavy (St 50) particles. *J. Fluid Mech.* **564**, 361–393.

KALLIO, G. A. & REEKS, M. W. 1989 A numerical simulation of particle deposition in turbulent boundary layers. *Intl J. Multiphase Flow* **15**, 433.

KHALITOV, D. A. & LONGMIRE, E. K. 2002 Simultaneous two-phase piv by two-parameter phase discrimination. *Exp. Fluids* **32**, 252–268.

KHALITOV, D. A. & LONGMIRE, E. K. 2003 Effect of particle size on the velocity correlations in turbulent channel flow. FEDSM45730, 445, ASME/JSME *Joint Fluid Engineering Conference*, Honolulu.

KHALITOV, D. A. & LONGMIRE, E. K. 2004 Gas–particle interaction in turbulent channel flow. *Tech Rep.* 2004-1. University of Minnesota.

KIGER, K. T. & PAN, C. 2002 Suspension and turbulence modification effects of solid particulates on a horizontal turbulent channel flow. *J. Turbul.* **3**, 1–21.

KROTHAPALLI, A., VENKATAKRISHNAN, L., LOURENCO, L., GRESKA, B. & ELAVARASAN, R. 2003 Turbulence and noise suppression of a high-speed jet by water injection. *J. Fluid Mech.* **491**, 131–159.

KULICK, J. D., FESSLER, J. R. & EATON, J. K. 1994 Prticle response and turbulence modification in a fully developed channel flow. *J. Fluid Mech.* **277**, 109–134.

KUMARAN, V. 1997 Velocity distribution function for a dilute granular material in shear flow. *J. Fluid Mech.* **340**, 319–341.

KUMARAN, V. 2003 Stability of a sheared particle suspension. *Phys. Fluids* **15**, 3625–3637.

KUMARAN, V. 2005 Kinetic model for sheared granular flows in the high Knudsen number limit. *Phys. Rev. Lett.* **95**, 108001.

KUMARAN, V. 2006 The constitutive relations for the granular flow of rough particles, and its application to the flow down an inclined plane. *J. Fluid Mech.* **561**, 1–42.

KUMARAN, V. & KOCH, D. L. 1993*a* Properties of a bidisperse particle – gas suspension. Part 1. Collision time small compared to viscous relaxation time. *J. Fluid Mech.* **247**, 623–642.

KUMARAN, V. & KOCH, D. L. 1993*b* Properties of a bidisperse particle – gas suspension. Part 2. Viscous relaxation time small compared to collision relaxation time. *J. Fluid Mech.* **247**, 643–660.

LI, Y. & MCLAUGHLIN, J. B. 2001 Numerical simulation of particle–laden turbulent channel flow. *Phys. Fluids* **13**, 2957.

LOURENCO, L. & KROTHAPALLI, A. 2000 True resolution piv: a mesh-free second order accurate algorithm. In *Proceedings of the 10th International Symposium on Applications of Laser Techniques in Fluid Mechanics Lisbon, Portugal*.

MCLAUGHLIN, J. B. 1989 Aerosol particle deposition in numerically simulated channel flow. *Phys. Fluids* A **1**, 1211.

NIEDERSCHULTE, M. A., ADRIAN, R. J. & HANRATTY, T. J. 1990 Measurements of turbulent flow in a channel at low Reynolds numbers. *Exp. Fluids* **9**, 222–230.

PAN, Y. & BANERJEE, S. 1997 Numerical investigation of the effects of large particles on wall-turbulence. *Phys. Fluids* **12**, 3786–3807.

PARIS, A. D. 2001 Turbulence attenuation in a particle–laden channel flow. PhD thesis, Stanford University.

PARIS, A. D. & EATON, J. K. 1999 Piv measurements in a particle–laden channel flow. In *Proceedings of the third ASME/JSME Joint Fluid Engineering Conference, San Francisco, CA* (ed. P. A. Pfund).

RASBAND, W. S. 2006 ImageJ Version 1.34 U.S. National Institute of Health Available at http://rsb.info.nih.gov/ij/.

SATO, Y. & HISHIDA, K. 1996 Transport process of turbulence energy in particle–laden turbulent flow. *Intl J. Heat Fluid Flow* **17**, 202–210.

SQUIRES, K. D. & EATON, J. K. 1990 Particle responce and turbulence modification in isotropic turbulence. *Phys. Fluids* A **2**, 1191.

SQUIRES, K. D. & EATON, J. K. 1991 Preferential concentration of particles by turbulence. *Phys. Fluids* A **3**, 1169.

SUZUKI, Y., IKENYA, M. & KASAGI, N. 2000 Simultaneous measurement of fluid and dispersed phases in a particle–laden turbulent channel flow with the aid of 3-D PTV. *Exp. Fluids* **29**, S185–S193.

TANAKA, T. & EATON, J. K. 2008 Classification of turbulence modification by dispersed spheres using a novel dimensionless number. *Phys. Rev. Lett.* **101**, 114502.

TANAKA, T. & EATON, J. K. 2010 Sub-Kolmogorov resolution partical image velocimetry measurements of particle–laden forced turbulence. *J. Fluid Mech.* **643**, 117–206.

TSUJI, Y. & MORIKAWA, Y. 1982 LDV measurements of an air–solid two-phase flow in a horizontal pipe. *J. Fluid Mech.* **120**, 385–409.

TSUJI, Y., MORIKAWA, Y. & SHIOMI, H. H. 1984 LDV measurements of an air–solid two-phase flow in a vertical pipe. *J. Fluid Mech.* **139**, 417–434.

UHLMANN, M. 2008 Interface-resolved direct numerical simulation of vertical particulate channel flow in the turbulent regime. *Phys. Fluids* **20**, 053305.

VREMAN, A. W. 2007 Turbulence characteristics of particle–laden pipe flow. *J. Fluid Mech.* **584**, 235–279.

WANG, Q. & SQUIRES, K. D. 1996 Large eddy simulation of particle–laden channel flow. *Phys. Fluids* **8**, 1207–1223.

YAMAMOTO, Y., POTTHOFF, M., TANAKA, T., KAJISHIMA, T. & TSUJI, Y. 2001 Large-eddy simulation of turbulent gas–particle flow in a vericle channel: effect of considering interparticle collisions. *J. Fluid Mech.* **442**, 303–334.

YANG, T. S. & SHY, S. S. 2005 Two-way interaction between solid particles and homogeneous air turbulence: particle settling rate and turbulence modification measurements. *J. Fluid Mech.* **526**, 171–216.

ZENG, L., BALACHANDAR, S., FISCHER, P. & NAJJAR, F. M. 2008 Interactions of a stationary finite-sized particle with wall turbulence. *J. Fluid Mech.* **594**, 271–305.